TECHNICAL ARTICLE

Microstructure and Mechanical Properties of Medium Manganese Steel with Different Aluminum Addition After Very Short Time Intercritical Annealing

Wei Ding, Nan Zhang, Guangying Zhang, Yan Li, and Min Zhang

In this work, the phase transformation, microstructure, and mechanical properties of medium manganese steels containing 1.0 and 2.5% aluminum (mass%) were investigated at different intercritical annealing (IA) temperatures (670-820 °C) after very short IA times (1 min) using thermodynamic simulations, scanning electron microscopy, transmission electron microscopy, x-ray diffraction and uniaxial tensile tests. The results show that with the addition of aluminum, the temperature range between A_1 and A_3 increases from 338 °C for 1.0% Al to 506 °C for 2.5% Al. The retained austenite (RA) has two different morphologies, namely polygonal and lath. Most of the RA transformed into martensite during deformation. Two types of martensite were observed: the α'-martensite and ε-martensite. The steel with 2.5% aluminum (mass%), after IA at 790 °C, shows the best combination of tensile properties, including a tensile strength of 982.5 MPa, an elongation of 42.96%, and tensile strength × total elongation greater than 42 GPa%.

1. Introduction

With the progress and development of science and technology, high-strength metal materials and their advanced processing methods are favored by researchers (Ref 1-4). The first-generation advanced high-strength steels (AHSS), such as dual-phase (DP) steel, transformation-induced plasticity (TRIP) steel, complex phase (CP) steel, and martensitic steel, cannot meet the increasing demands of the automobile industry due to their low strength–ductility balance (10-20 GPa%) (Ref 5, 6). At the same time, the second generation AHSS exhibits excellent mechanical properties, the product of tensile strength and elongation reaches 50-70 GPa %, including Hadfield steel and twin induced plasticity (TWIP) steel (Ref 5, 7). In recent years, the third generation of advanced high-strength steel (AHSS), with a good balance of strength and ductility, has been developed globally, which is the product of the ultimate tensile strength (TS) and total elongation (TEL), estimated to be ≥ 30 GPa% (Ref 2). One of the most promising third-generation AHSS is the medium manganese steel, which is a steel with a manganese concentration of between 3.0 and 10.0 mass% (Ref 8, 9). It has attracted significant research attention due to its excellent mechanical properties, relatively low material cost and industrial feasibility. Medium manganese steel achieves excellent mechanical properties as a result of the transformation-induced plasticity (TRIP) effect of the RA (Ref 10-12). Therefore, between the α + γ / α + γ + θ region, a brief heat treatment such as IA, also known as reverted transformation from martensite to austenite, has been used to produce the duplex structure of ultrafine ferrite and austenite (Ref 13).

The stability of austenite plays an essential role in maximizing elongation through the TRIP effect (i.e., an enhanced elongation due to the formation of martensite during deformation, which increases the work-hardening rate and, thus, delays necking (Ref 14, 15)). As a stable element of RA, the content of carbon and manganese directly affects the stability of RA. During intercritical annealing, carbon diffuses rapidly into RA as an interstitial atom, while the diffusion rate of Mn is comparatively slow (Ref 16). Aluminum is known to raise the A_3 temperature and enlarge the austenite–ferrite intercritical range, thus shortening the IA time and expanding the processing window (Ref 17). Previous studies have found that excellent mechanical properties can be obtained with a short annealing duration (Ref 18-21), and producing medium-manganese steels with aluminum addition has great potential for steel density reduction (Ref 22). Furthermore, aluminum promotes the formation of inhibiting layers, thereby improving the coating qualities of steels (Ref 23). However, the addition of too much aluminum can affect the quality of steel and even cause it to be scrapped, such as increased aluminum impurities and decreased continuous casting speed (Ref 24). Therefore, the content of aluminum needs to be adequately controlled.

Wei Ding, Nan Zhang, and **Guangying Zhang**, School of Material and Metallurgy, Inner Mongolia University of Science and Technology, Baotou 014010, People's Republic of China; **Yan Li**, School of Material and Metallurgy, Inner Mongolia University of Science and Technology, Baotou 014010, People's Republic of China; and Collaborative Innovation Center of Integrated Exploitation of Bayan Obo Multi-Metal Resources, Inner Mongolia University of Science and Technology, Baotou 014010, People's Republic of China; and **Min Zhang**, School of Mechanical, Electronic and Control Engineering, Materials Science and Engineering Research Center, Beijing Jiaotong University, Beijing 100044, People's Republic of China. Contact e-mails: kenshin110@163.com and zhangm@bjtu.edu.cn.

This research has investigated the microstructure and mechanical properties of two medium manganese steels with different aluminum contents (1.0 and 2.5 aluminum (mass %)) after a very short IA time of 1 min at different temperatures. The excellent mechanical properties and the microstructure evolution during the deformation of 2.5 aluminum steel were also discussed.

2. Materials and Methods

2.1 Materials

Based on Fe-0.2C-5.0Mn-0.5Si (mass %), 1.0 and 2.5 aluminum (mass %) were added as the nominal composition, named 1.0 Al and 2.5 Al, respectively. The compositions of 1.0 Al and 2.5 Al cast ingots prepared by vacuum induction melting are Fe-0.19C-5.35Mn-0.95Al-0.51Si (mass %) and Fe-0.19C-5.25Mn-2.45Al-0.50Si (mass %), respectively. The ingots were solution treated at 1200 °C for 60 min, hot-rolled into 3.5-mm-thick plates at approximately 950 °C, cooled to and maintained at 600 °C for 1.5 h, and, subsequently, a coiling process is simulated by furnace cooling to room temperature. After surface descaling, the plates were further cold-rolled to 1.4-mm-thick sheets (60% reduction) at room temperature. By FactSage® 8.0 software and FSstel databases, the transformation temperatures (A_1, A_{cm}, A_3) were calculated as 467, 644, and 805 °C for the 1.0 Al, respectively, and 510, 674, and 1016 °C for the 2.5 Al, respectively. The calculation was performed using the nominal compositions of 1.0 Al and 2.5 Al. The specimens with 25 * 100 mm size were taken from the cold-rolled sheet and annealed intercritically in a salt bath for 1 min for microstructure observation and mechanical properties testing. The heat treatment mentioned above is shown in Fig. 1.

2.2 Procedures

The microstructure of the samples before and after fracture was observed under scanning electron microscope (SEM, GeminiSEM300) and field-emission transmission electron microscope (TEM, JEM-2010). Specimens for SEM observation were electro-etched in a solution of 85 vol.% ethanol and 15 vol.% perchloric acid after mechanically polishing (Ref 25).

Specimens for TEM observation were mechanically ground to a thickness of 50 μm, punched into 3 mm diameter, and then electro-polished in a twin-jet polisher with a solution of 95 vol.% acetic acid and 5 vol.% perchloric acid at − 20 °C.

The volume fractions of RA were determined by x-ray diffraction (XRD, Bruker D8 ADVANDE) using a cobalt target. Specimens for XRD were electro-polished at 15 V in a solution of 90 vol.% ethanol and 10 vol.% perchloric acid at room temperature after mechanically polishing. The integrated intensities (I) of the (200) and (211) peaks of ferrite / martensite (bcc) and the (200), (220) and (311) peaks of RA (fcc) were determined by least-square fitting of a Pearson VII type function. The volume fraction of RA(V_γ) was then calculated by Formula 1 (Ref 26):

$$V_\gamma = \left[\frac{1}{q}\sum_{j=1}^{q}\frac{I_{\gamma j}}{R_{\gamma j}}\right] \bigg/ \left[\frac{1}{q}\sum_{j=1}^{q}\frac{I_{\gamma j}}{R_{\gamma j}} + \frac{1}{p}\sum_{i=1}^{p}\frac{I_{\alpha i}}{R_{\alpha i}}\right] \times 100\% \qquad (Eq\ 1)$$

Here, q represents the number of austenite peaks, R represents the calculated theoretical intensity for a certain peak, and p represents the number of ferrite/martensite peaks.

The dog-bone-shaped tensile specimens with a width of 6.5 mm and a gauge length of 25 mm along the rolling direction, were fabricated and heat-treated. The tensile tests were carried out by a CMT universal tensile machine with an initial load of 20 N and a stretching speed of 2 mm / min.

3. Results

3.1 Influence of Aluminum on Equilibrium Phase Fractions

Figure 2(a) and (b) shows the calculated phase fractions for 1.0 Al (Ref 21) and 2.5 Al after IA, as well as the experimentally measured RA contents. Ferrite (F), RA, Cementite (CEME) and Martensite (M) are abbreviations used to describe the four phases.

Four intercritical temperatures are shown in Fig. 2, representing the temperature at which austenite begins to precipitate (A_1), the temperature at which the austenite transformation is complete (A_3), the temperature at which the cementite is completely dissolved (A_{cm}) and an IA temperature, where the M_S of the reversed austenite equals room temperature of 20 °C
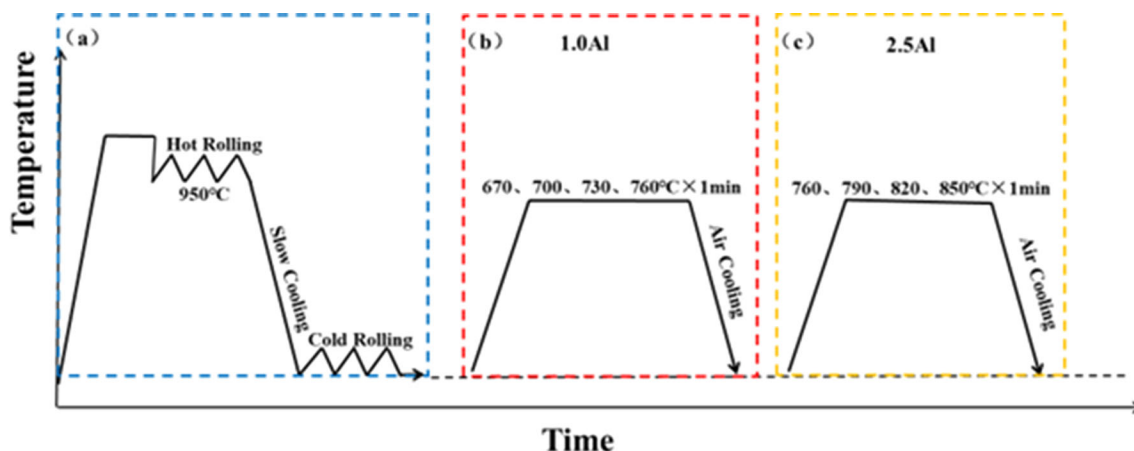
Fig. 1 Process flow diagram of 1.0 Al and 2.5 Al medium manganese steel. Process flow diagram of 1.0 Al and 2.5 Al medium manganese steel. (a) is rolling process, (b) is 1.0 Al annealing process, (c) is 2.5 Al annealing process
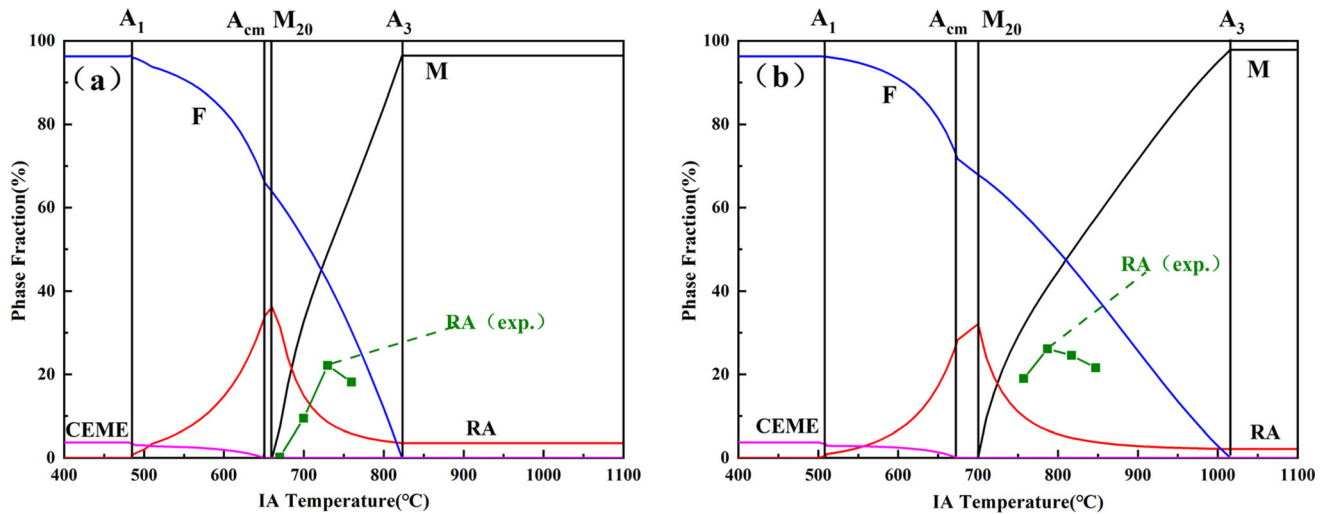
Fig. 2 Calculated phase fractions of ferrite (F), cementite (CEME), and martensite (M) for the (a) 1.0 Al (Ref 21) and (b) 2.5 Al annealed at different temperatures using the FactSage®8.0 with FSstel databases and an RA prediction model (Ref 28-30)

(M_{20}) (Ref 27, 28). When annealing at temperatures greater than A_3, most of the RA transforms into fresh martensite during quenching. Cementite remains when annealing at temperatures lower than A_{cm}. The RA is completely stabilized by solute partitioning when annealing at temperatures below M_{20}, whereas no martensite is present at room temperature.

Intercritical temperature increases with increasing aluminum content. The greatest increase is seen in the A_3 temperature, which raise from 805 °C for 1.0 Al to 1016 °C for 2.5 Al. This causes the temperature range between A_1 and A_3 to increases from 338 °C for 1.0 Al to 506 °C for 2.5 Al; range shifts to higher temperatures. Additionally, the difference between the M_{20} and A_{cm} temperatures increases from 19 °C for 1.0 Al to 36 °C for 2.5 Al. Predicted RA values reach their maximum at the M_{20} temperature, with 36.1% for 1.0 Al and 30.8% for 2.5 Al. However, measured RA values were slightly lower, with the maximum RA being 22.1% for 1.0 Al and 25.8% for 2.5 Al, and the corresponding annealing temperatures were 730 and 790 °C, respectively, for 1.0 Al and 2.5 Al. Compared with the predicted values, the maximum RA values measured are lower, whereas annealing temperatures are higher.

3.2 Microstructure

Figure 3 depicts the microstructures of the investigated steel before the tensile test. Microstructures of the 1.0Al and are shown in (a), (b), (c), (d), and (e), while those of the 2.5 Al are shown in (f), (g), (h), (i), and (j).

For the 1.0 Al, there is little difference in the microstructure after IA at temperatures between 670 °C and 700 °C which is composed of F, RA, and CEME, as shown in Fig. 3(a)–(c), respectively. With an increase in the annealing temperature, CEME dissolves and the RA increases gradually. At IA temperatures of 730 °C (Fig. 3d), the RA increases significantly, whereas some CEME particles coarsen, which is consistent with the phenomenon observed in the previous modeling (Ref 10). When the IA temperature increases to 760 °C, CEME particles completely disappear and martensite appears in the microstructure (Fig. 3e).

With the increase in IA temperature, the microstructure of 2.5Al evolves in a similar manner to that of 1.0Al. Note that

delta ferrite (δ-Fe) appears in 2.5 Al, which is a high-temperature phase-genetic structure caused by high aluminum content that contributes to the stability of delta ferrite. In comparison to 1.0 Al, 2.5 Al is annealed at a higher temperature, making it less likely to form CEME phase when IA temperature reaches 760 °C. At this temperature, the microstructure includes ferrite, δ-Fe, RA, and CEME phases (Fig. 3f). When the IA temperature further increases to 790 °C-820 °C, the CEME phase disappears, but the other three phases unchanged (Fig. 3g and h). Finally, when the IA temperature increases to 850 °C, martensite appears in the microstructure (Fig. 3i and j).

An increase in aluminum content leads to an increase in IA temperature. While the temperature of Acm only increases by 30 °C under equilibrium conditions, the temperature difference between full dissolution of the CEME phase and formation of the new martensite phase (i.e., the interval between A_{cm} and M_0) is larger. For 2.5 Al, the CEME phase exists at an IA temperature of 760 °C, and the fresh martensite phase appears at 850 °C. At IA temperatures between 790 and 820 °C, neither the CEME phase nor the martensite phase are present. It is possible to achieve the best mechanical properties when annealing temperature between this range. In comparison, for 1.0 Al, the CEME phase exists after IA at 640-730 °C. When the annealing temperature is increased to 760 °C, the CEME phase disappears and the fresh martensite phase appears. For 1.0 Al, there is no such nominal interval annealing temperature.

Figure 4(a) shows the XRD diffraction patterns after IA at different temperatures. The RA contents at different IA temperatures were calculated using Eq 1, as shown in Fig. 4(b). With regard to the 1.0Al and 2.5Al, a tendency of the volume fraction of RA increasing at first and then decreasing as the IA temperature rises is observed. The maximum volume fraction of the RA can be obtained when IA occurs at 730 °C and 790 °C for 1.0 Al and 2.5 Al, respectively. It is consistent with the observation of microstructure shown in Fig. 3(d) and (h), respectively.

At temperatures of 670 °C and 700 °C, there is little difference in the microstructure of 1.0% Al. The volume fraction of RA is below 5% when IA at 670 °C, and increases to around 10% when IA at 700 °C. This indicates that the CEME
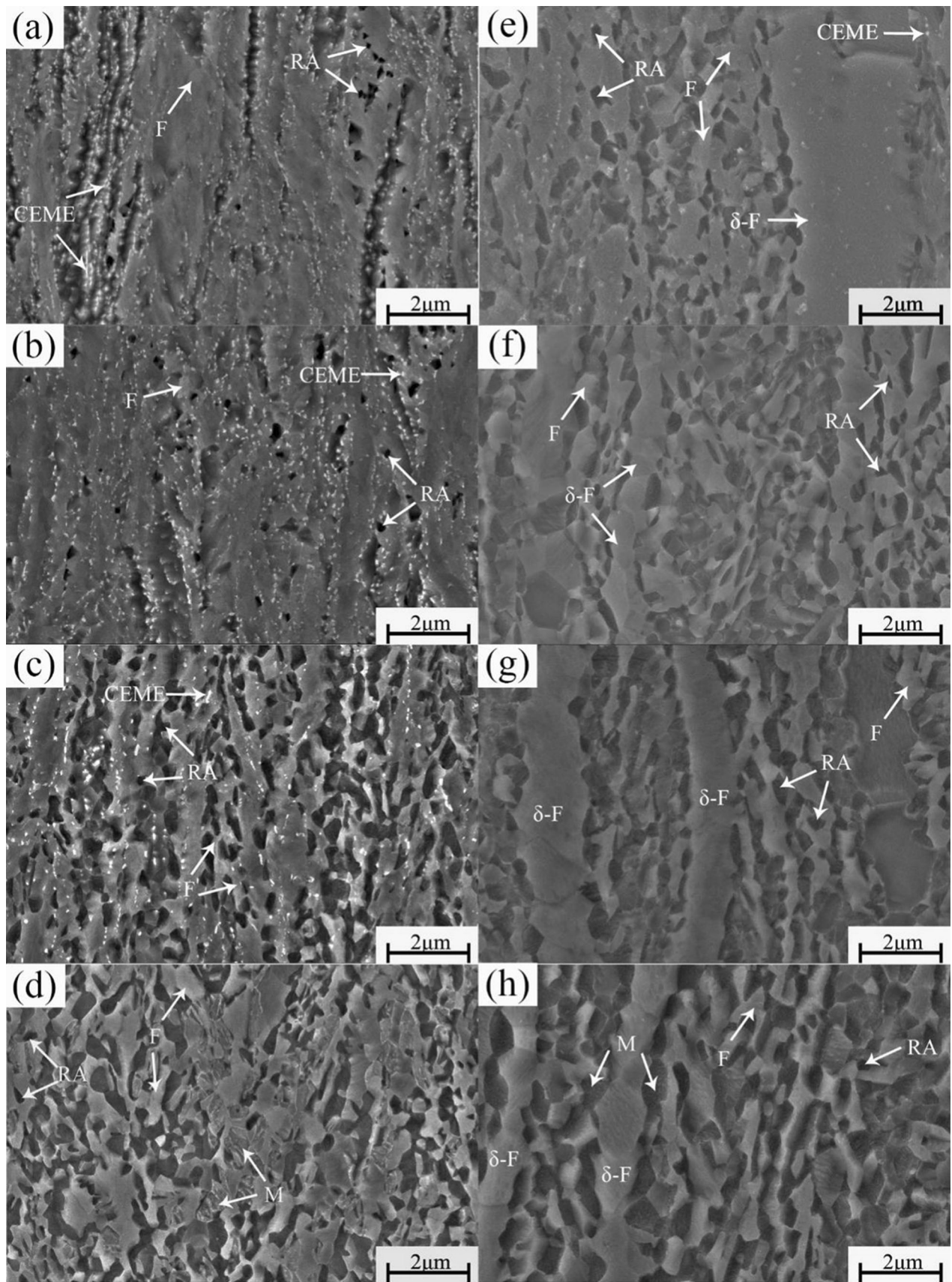
Fig. 3 SEM micrographs of the investigated steels before the tensile test. The IA temperatures are (a) 670 °C, (b) 700 °C, (c) 730 °C, and (d) 760 °C for 1.0 Al and (e) 760 °C, (f) 790 °C, (g) 820 °C, and (h) 850 °C for 2.5 Al. F, RA, CEME, and δ-F denote ferrite, retained austenite, cementite, and delta ferrite, respectively
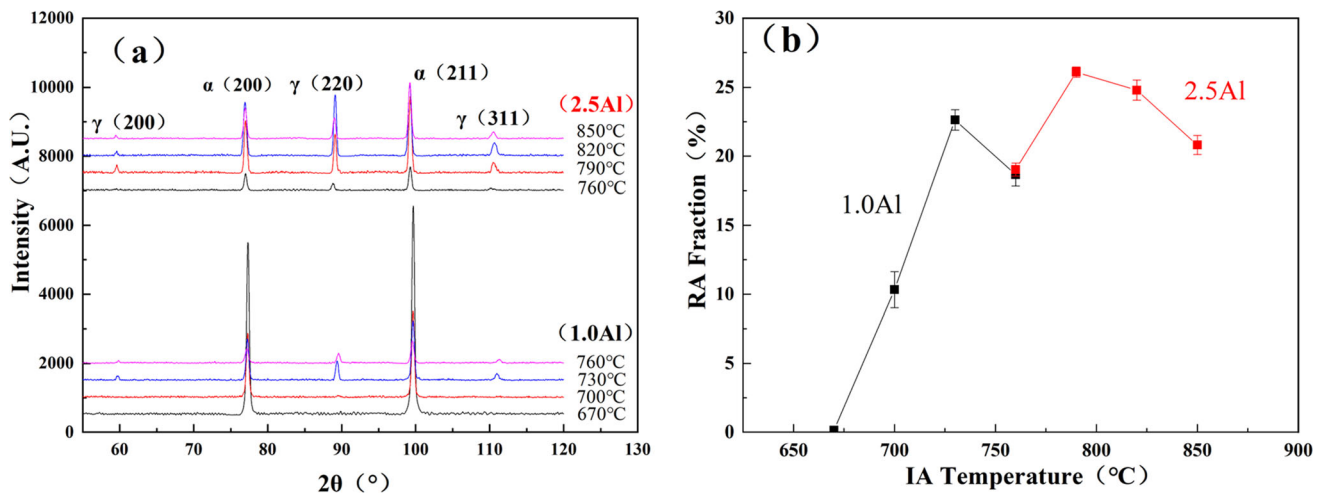
Fig. 4 XRD results and the RA fraction after IA, (a) is the diffraction pattern, (b) is the calculated RA contents by XRD patterns

phase dissolves and RA increases gradually as the IA temperature increases. However, when the IA temperature further increases to 760 °C, the fraction of RA decreases, corresponding to the appearance of the fresh martensite phase. This is due to the insufficient concentrations of carbon and manganese to sustain the stability of the reverted austenite as the IA temperature rises to 760 °C, resulting in the appearance of fresh martensite in the subsequent cooling process.

For 2.5 Al, it can be seen from the morphological observation that the maximum austenite fraction may appear in the samples when IA at 790 °C-820 °C. At this range of temperature, the CEME disappears, but fresh martensite cannot be observed. As shown in Fig. 4(b), the maximum RA fraction obtained after IA at 790 °C was 25.8%, which is reduced when IA at 820 °C. The fresh martensite phase cannot be observed in the morphology observation (Fig. 3h). In comparison, the maximum RA value in the 2.5 Al (Fig. 4) is greater than that in the 1.0 Al (Fig. 2), which is contrary to the calculation result. This is likely due to the higher IA temperature accelerating the diffusion of Mn, resulting in higher RA stability and greater RA volume fraction in the 2.5 Al at room temperature.

It can be concluded that the 2.5 Al is more suitable for the continuous annealing process than the 1.0 Al, especially for short-time annealing conditions.

3.3 Mechanical Properties

Figure 5 displays the engineering stress–strain curves of 1.0 Al and 2.5 Al. It is clear that annealing temperature significantly affects the tensile deformation. There are three different characteristics of stress–strain curves depending on the IA temperature. For 1.0 Al, IA at lower temperatures (670, 700 °C), the stress–strain curve shows a small total TEL and extremely low strain-hardening behavior. IA at 730 °C, the stress–strain curve exhibits longer yield point elongation with a higher TEL. IA at 760 °C, the stress–strain curve shows a discontinuous yield with high strain-hardening behavior. Similar stress–strain curves were also obtained in 2.5 Al.

Figure 6 displays the variation of TEL, TS, yield strength (YS), and TS × TEL with annealing temperature for the 1.0 Al and 2.5 Al.

As the annealing temperature increased, the TEL of 1.0 Al and 2.5 Al first increased to peak value of 29.76% at 730 °C

and 42.96% at 790 °C, respectively, and then decreased, as shown in Fig. 6(a). This is due to the fact that at apposite annealing temperatures (730 and 790 °C for 1.0 Al and 2.5 Al, respectively), a large amount of RA exhibits a remarkable TRIP effect, promoting elongation during deformation. At lower annealing temperatures, (670-700 and 760 °C for 1.0 Al and 2.5 Al, respectively), the microstructure consists mainly of tempered martensite, while the RA fraction is low (approximately less than 10% for the 1.0 Al and less than 15% for the 2.5 Al), leading to an insignificant TRIP effect. At higher annealing temperatures (760 and 820 -850 °C for 1.0 Al and 2.5 Al, respectively), grain growth, average carbon, and manganese content decrease, decreasing the stability of the reverted austenite. This means that most of the reverted austenite will transform to martensite during cooling, thereby reducing the elongation of the material.

As the temperatures increases, the TS of 1.0 Al initially declines, then rises again. The initial decrease is attributed to the recovery of the ferrite matrix at low annealing temperatures. However, as the annealing temperature increases, a large amount of the reversed transformation from austenite to martensite during cooling, which increases the TS. The same reason explains the variation in the TS of 2.5 Al. However, in the case of 2.5 Al, the TS increased continuously with an increase in temperature, as shown in Fig. 6(b).

As shown in Fig. 6(b), the yield strength (YS) of 1.0A and 2.5A decreased as the temperature increased, with minimum values of 742.39 MPa at 760 °C and 729.82 MPa at 880 °C, respectively. It is thought that this decrease in YS with rising IA temperature is due to grain recovery and/or recrystallization, martensite formation and RA stability. As the IA temperature increases, grain growth occurs and dislocation density decreases, which can facilitate dislocation slip and reduce YS. As the temperature further increases, martensite forms during cooling, leading to volume expansion and creation of compressional stresses in the surrounding regions of martensite islands. These stresses act as back stresses, further reducing YS. In addition, as increasing IA temperature, the yielding of the unstable RA is initiated by stress-induced transformation. The combination of the internal compressive stresses and the stress-induced transformation helps to reduce YS significantly.

Compared to 2.5 Al, 1.0 Al had a significant TS of 1116-364 MPa. However, its TEL was lower than that of 2.5 Al.
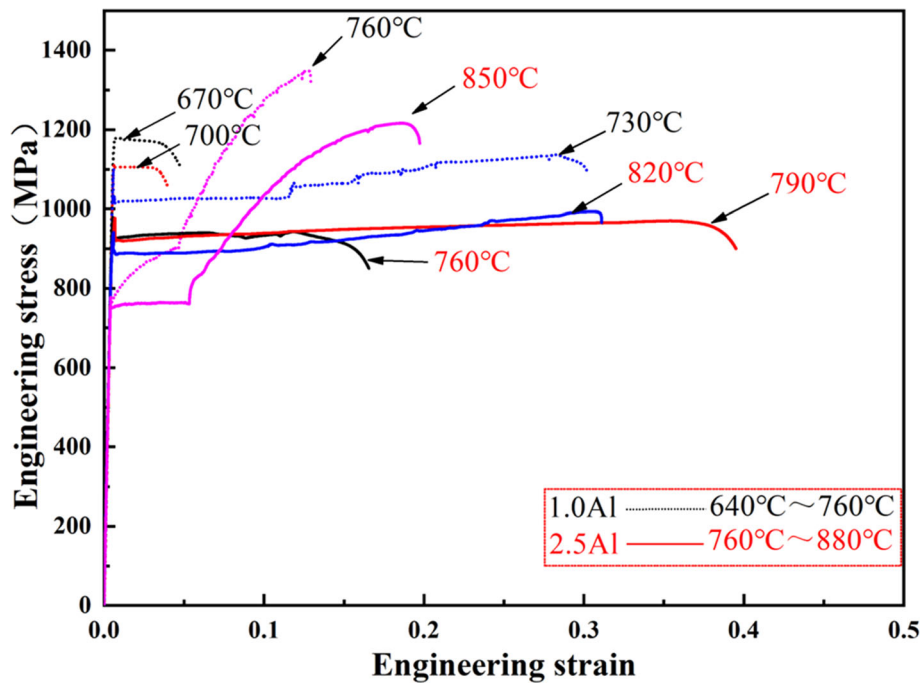
Fig. 5 Engineering stress–strain curve of the 1.0 Al and 2.5 Al after annealing
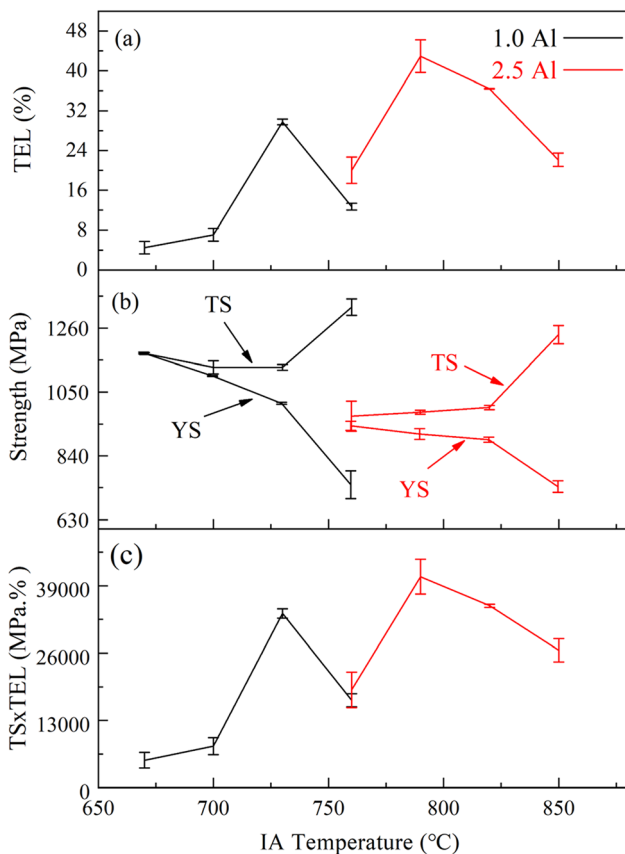

Fig. 6 Mechanical properties of the 1.0 Al and 2.5 Al at different annealing temperatures

With the addition of Al, there was an observable change in the microstructures of the investigated steels; delta ferrite appeared in the microstructure. Delta ferrite is softer than RA and yields before RA. The appearance of delta ferrite phase is bound to increase the plasticity of steel (Ref 31). If the softening effect of delta ferrite is stronger than that of phase transformation strengthening, the strength of steel will significantly decrease. Therefore, the content of delta ferrite should be reasonably controlled to achieve an optimal combination of strength and plasticity. In addition, the appropriate content of delta ferrite also increases the content of RA, which is consistent with the results of Fig. 4. Among all investigated steels, 2.5 Al IA at 790 °C exhibited optimal mechanical properties, with a TS of approximately 1000 MPa, a TEL of approximately 43.00%, and TS × TEL greater than 42 GPa%.

Figure 7 displays the work hardening rates and true stress / true strain plots for 1.0 Al (730 °C) and 2.5 Al (790 °C). It can be determined that for both samples, there are three distinct stages of work hardening prior to necking.

Stage I can be identified by a sharp drop in work-hardening rate and is usually present in almost all steels, independent of its microstructure (Ref 32). The rapid decrease of hardening rate is mainly related to the glide of dislocation in a single system. Stages II and III, on the other hand, demonstrate different work hardening rates for the two samples. The 1.0Al (730 °C) sample shows a rapid increase in the work hardening rate in stage II, followed by a swift decline in stage III. The emission of dislocations interacts with slip of other dislocations (Ref 33) and may even lead to cross-slip (Ref 34), which increases work hardening rate. It must be noted, however, that this is not the only factor leading to an improved work hardening. During deformation, the RA is transformed into martensite, which strengthens the local region and inhibits the nucleation and growth of microcracks and/or microvoids (Ref 35). Meanwhile, the newly formed martensite also contributes to improved work hardening. Stage III exhibits a reduction in the work-hardening rate caused by the dislocation annihilation rate which is greater than the dislocation multiplication rate caused by the TRIP effect and / or sliding dislocations.
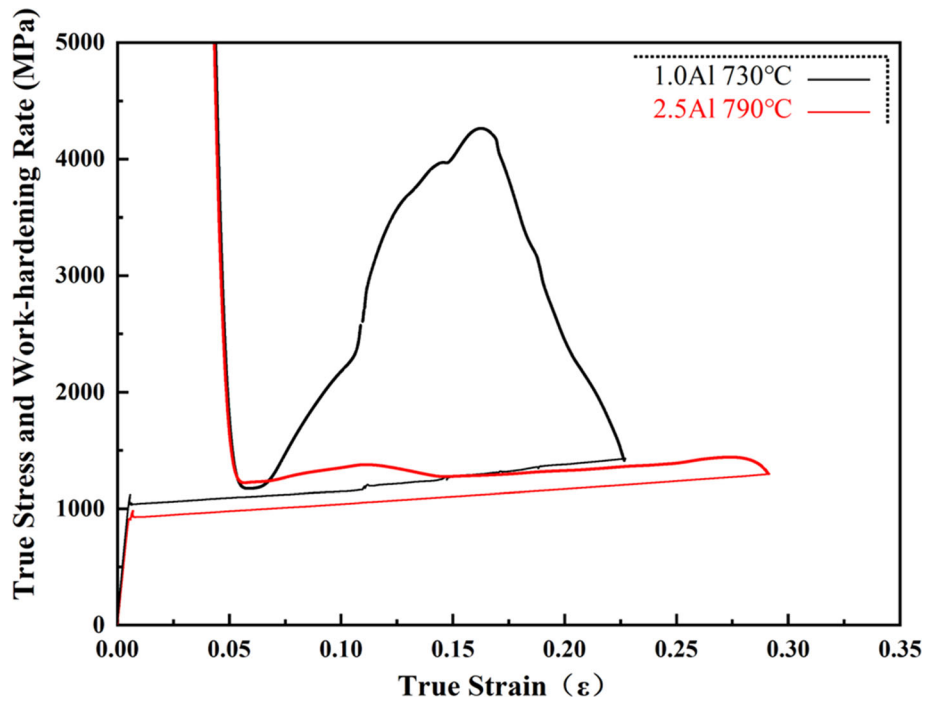
Fig. 7 Work-hardening rate (dσ / dε) in the 1.0 Al at 730 °C and 2.5 Al 790 °C

Interestingly, the work hardening of 2.5 Al (790 °C) only slightly increased in stage II, and work hardening did not decrease significantly in stage III. The work-hardening behavior in stage II is similar to that of twining-induced plasticity steel with high SFE and small grain size (Ref 33). Many reports in the literature describe a dramatic increase in SFE caused by aluminum addition (Ref 36). In stage III, the TRIP effect of RA increases works hardening, which can partially offset the decrease in work hardening caused by dislocation annihilation.

4. Discussion

4.1 Excellent Mechanical Properties of 2.5 Al After Annealed in a Very Short Time

References for steel and their mechanical properties after IA from different literature are plotted and briefly compared in Fig. 8 (Ref 10, 13, 21, 37-42). Compared to the literature, the studied 2.5 Al can show excellent mechanical properties in a very short IA time (1 min) due to the addition of aluminum. In particular, the strength × ductility is over 42 GPa % for IA at 790 °C, which meets the requirement of 30 GPa% for the third generation AHSS used in the automotive industry (Ref 2). Compared with Hadfield steel, 2.5Al has similar strength and plasticity, but 2.5Al has a higher yield strength.

4.2 Microstructure Evolution of 2.5 Al After Tensile Test

Figure 9 and 10 shows microstructures and RA of the 2.5 Al before and after the tensile test, respectively.

After the tensile test, the ratio of martensitic transformation in the RA of the sample at 760 °C was relatively low (only 70%). This indicates that the RA stability of this sample is high
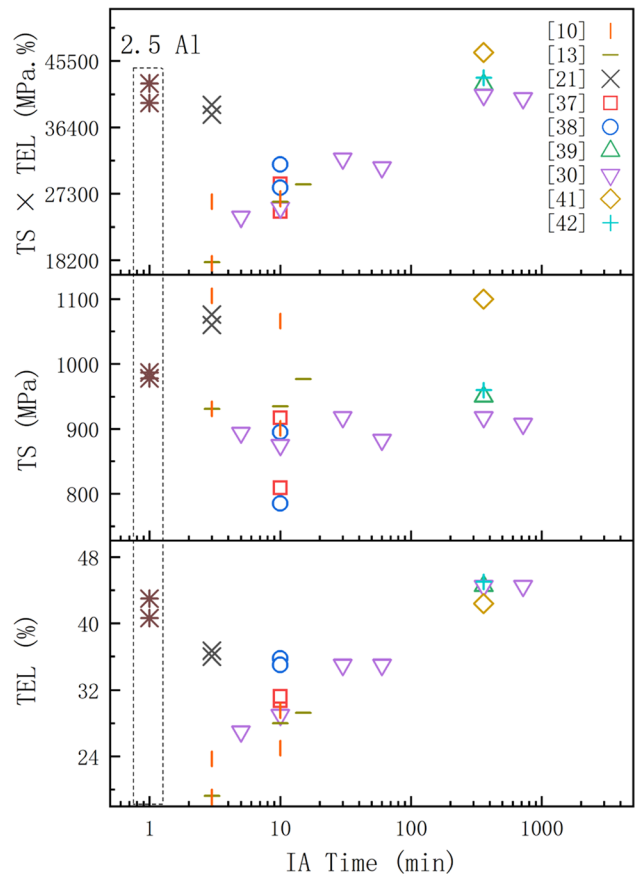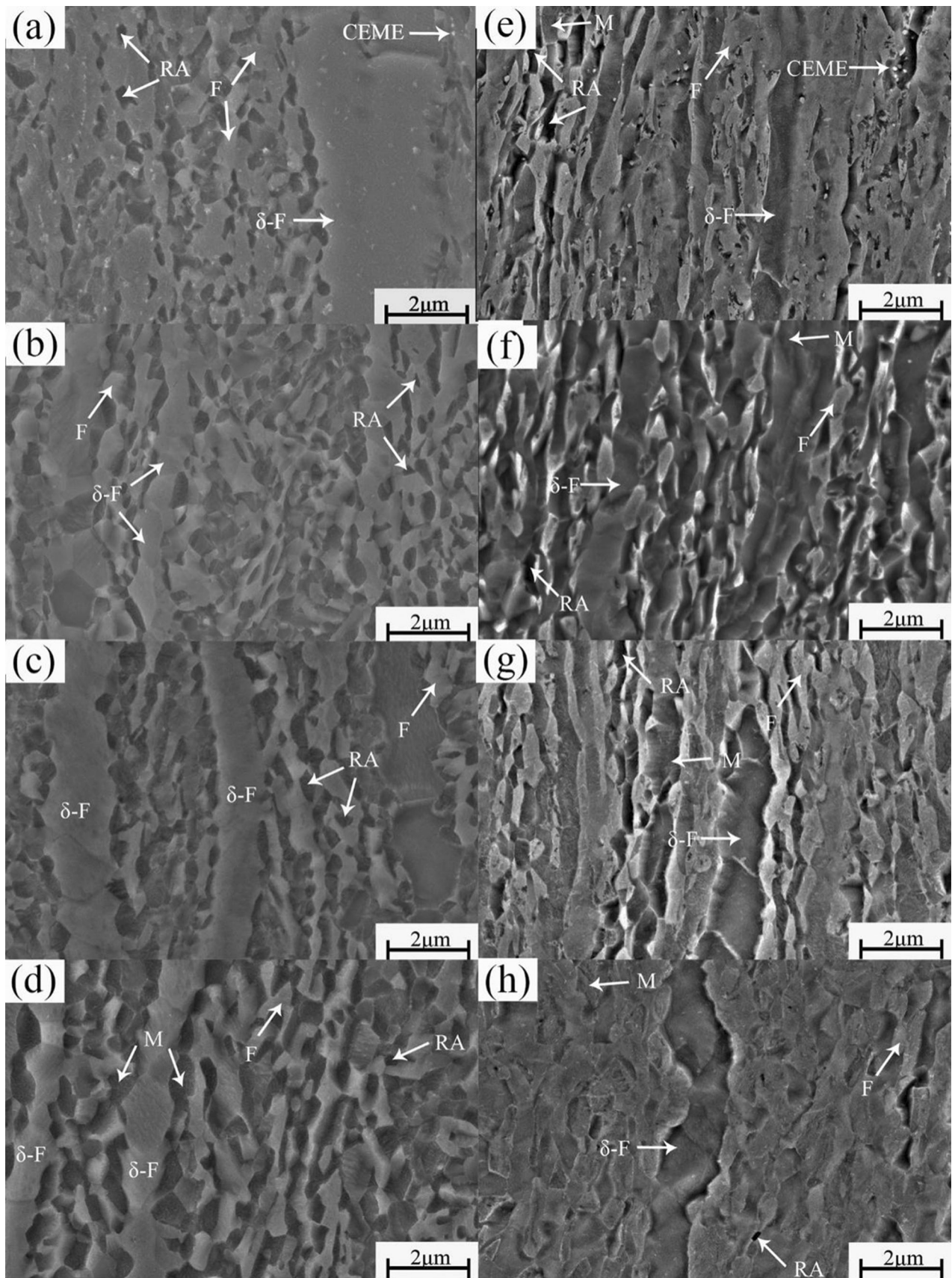

Fig.8 Variation of mechanical properties of 2.5 Al steel with short IA time (1 min) compared to literature
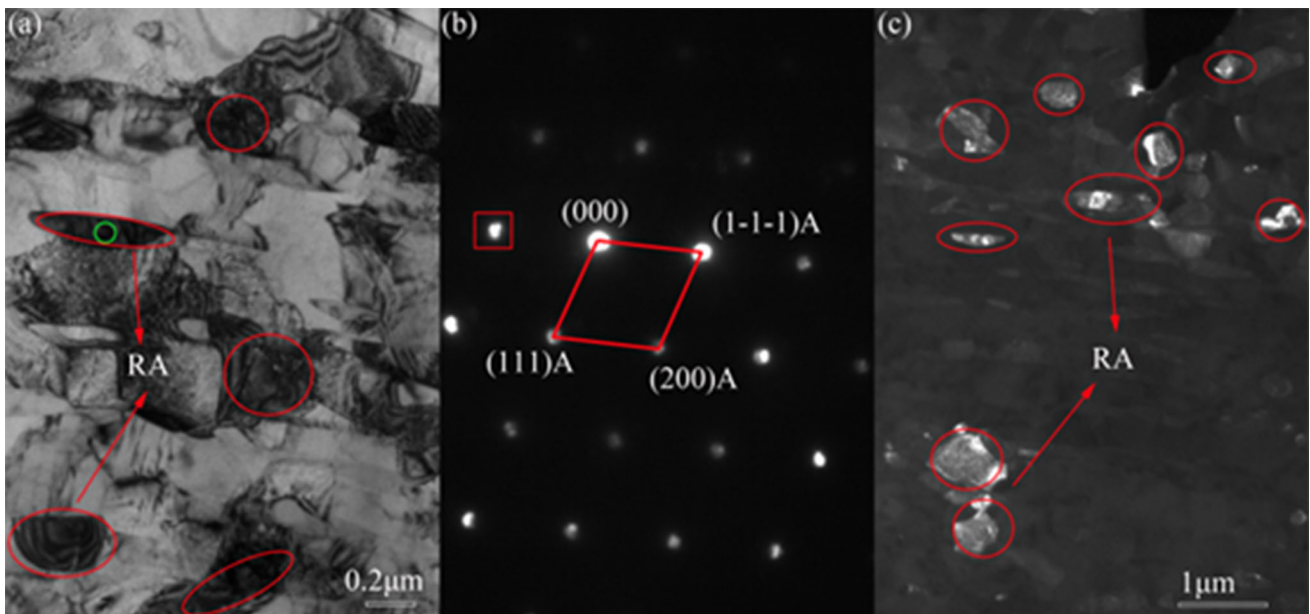
Fig. 9 SEM micrographs of the 2.5 Al. The IA temperatures are as follows: (a), (e) 760 °C, (b), (f) 790 °C, (c), (g) 820 °C, and (d), (h) 850 °C. The micrographs in (a), (b), (c), and (d) show the samples after IA; those in (e), (f), (g), and (h) show those after stretching. F, RA, C and δ-F represent ferrite, RA, cementite and delta ferrite respectively
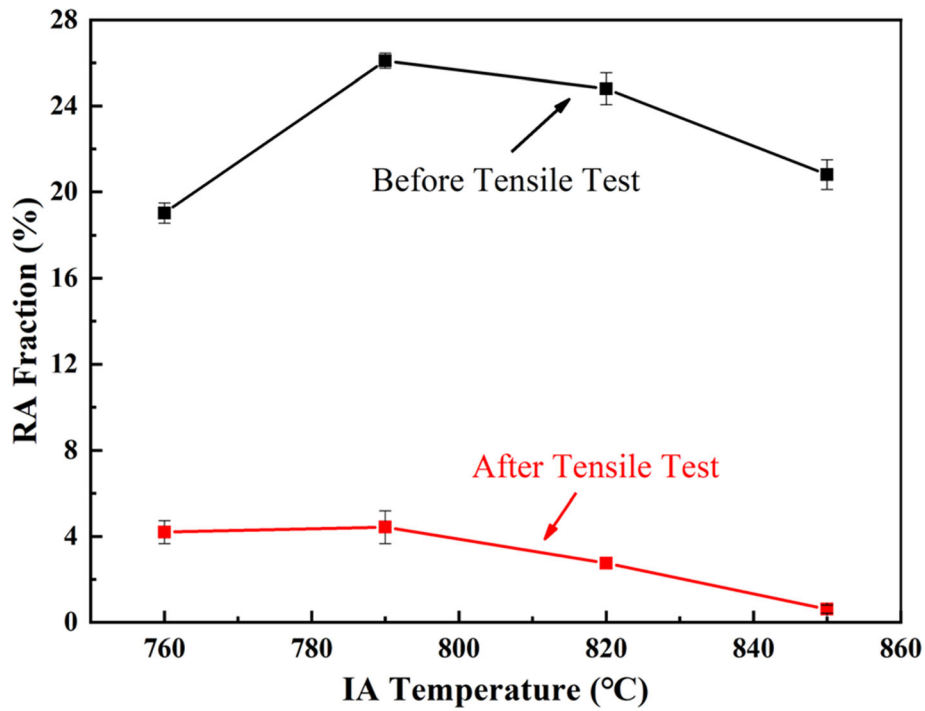
Fig. 10 Volume fraction of the RA of the 2.5 Al steel before and after the tensile test


Fig. 11 RA before the tensile test (790 °C). (a) Bright-field image; (b) diffraction pattern of the green circle region in (a); (c) dark field image of red rectangle in (b)

and the TRIP effect is not reflected, resulting in the low TEL at 760 °C. However, when the sample was heated to between 790 °C and 850 °C, its fractured microstructure experienced great deformation along the tensile direction, with a large amount of RA transformed into martensite. Notably, the sample at 790 °C had not only the largest amount of RA transformed into martensite, but also had a transformation rate as high as approximately 83%. This means that the sample had a more significant TRIP effect and can obtain better mechanical properties.

TEM was used to investigate the deformation of austenite of 2.5 Al after IA at 790 °C in more detail. Figure 11 shows the TEM image after IA, and the results of the interrupted tensile test specimen are shown in Fig. 12 and 13.

As shown in Fig. 11, there are two different morphologies of RA before the tensile test. The first is the polygonal RA with a grain size of approximately 200-800 nm, and most grains were smaller than 500 nm. The second morphology is the lath RA with a width of approximately 100 nm. The stability of the RA was influenced not only by the chemical composition, but
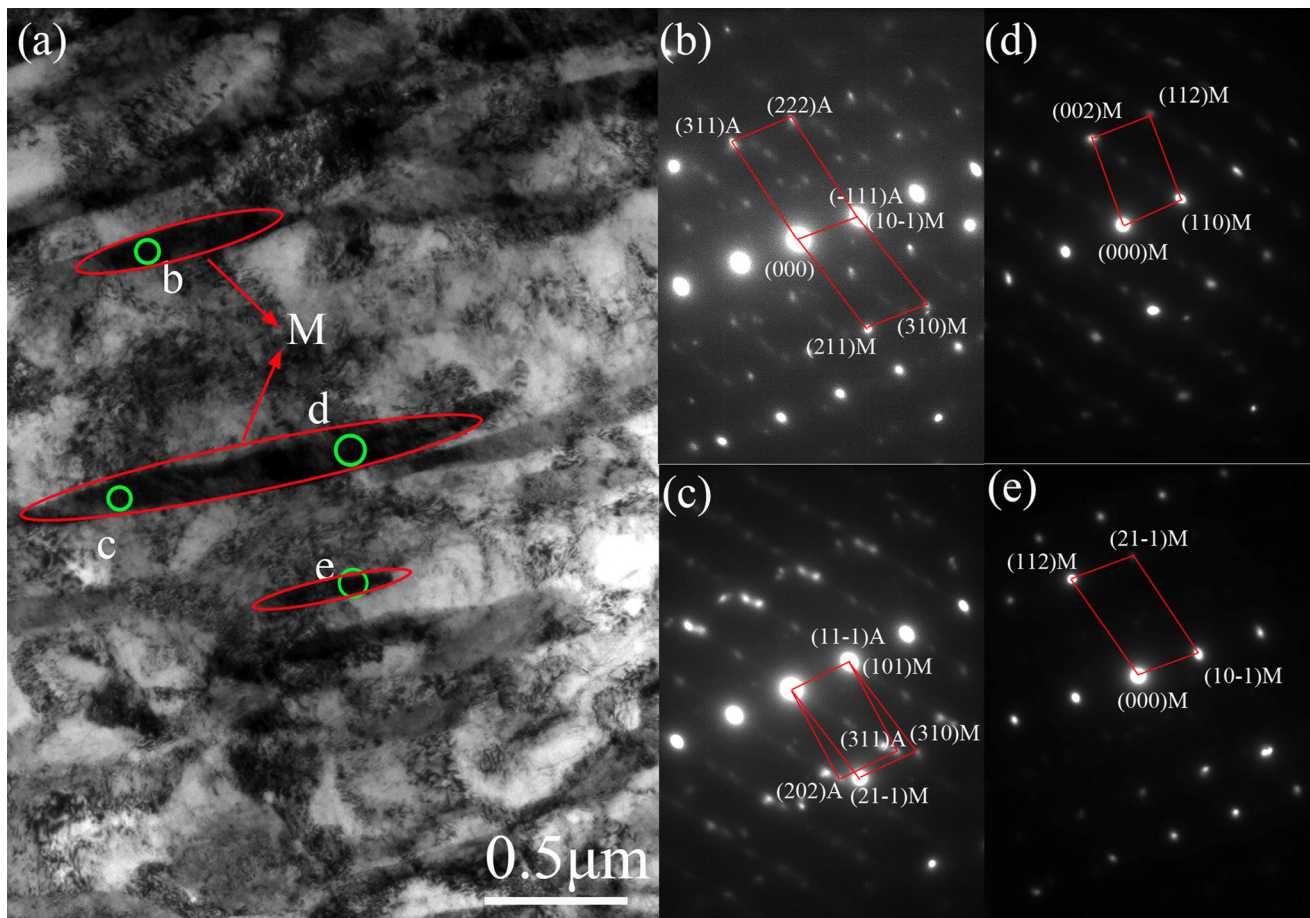
Fig. 12 RA transformed into martensite (α'-martensite) after fracture (790 °C). (a) TEM bright field image; (b) diffraction pattern of green circle b in (a); (c) diffraction pattern of green circle c in (a); (d) diffraction pattern of green circle d in (a); (e) diffraction pattern of green circle e in (a)
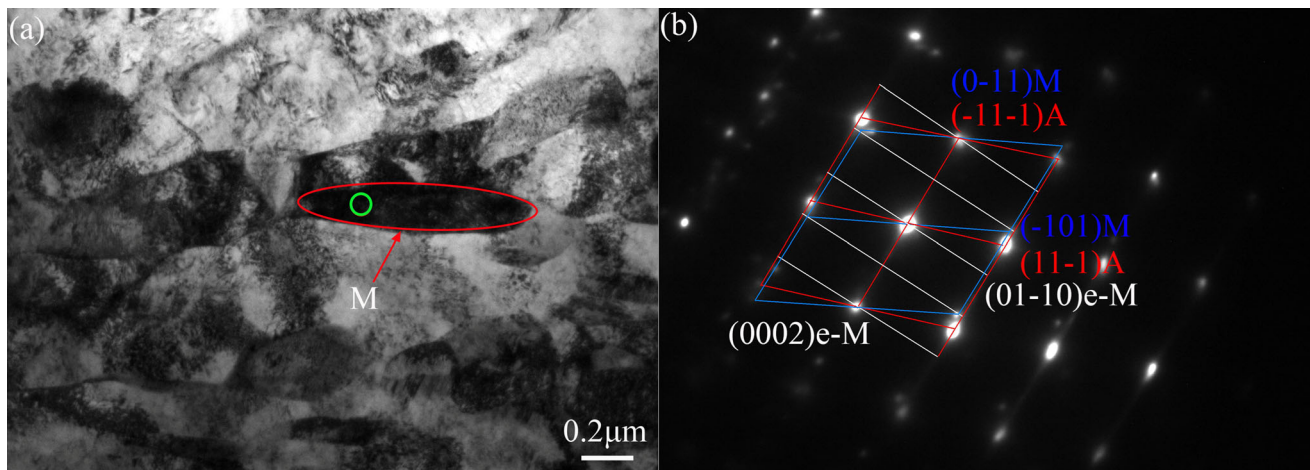
Fig. 13 RA transformed into martensite (α'-martensite) and e-M (ε-martensite) after fracture (790 °C). (a) TEM bright field image; (b) diffraction pattern of the green circle in (a)

also by the size and morphology of grains (Ref 43, 44). It has been found that the smaller the RA grain size, the better its stability (Ref 45). In addition, the lath RA is more stable than the polygonal morphology (Ref 46). During the tensile test, the polygonal RA with coarse grains would transform into martensite at the early stage due to its poor stability. On the other hand, the polygonal RA with fine grains and the lath RA transform into martensite at the middle or late tensile deformation stage. Comparing the stabilities of the two different RA morphologies, the high stabilities of lath RA allow it to be maintained at higher strains compared to the polygonal microstructure. That is, at higher strains, there will be some

lath RA that can be used for martensite transformation to continuously produce the TRIP effect, whereas the polygonal RA would have exhausted its TRIP effect. These RA transformations to martensite during tensile deformation are inferred to be the main reason for the excellent mechanical properties of the investigated samples (Ref 47).

For the interrupted tensile test specimen, the RA transformed into martensite, i.e., a strain-induced austenite–martensite transformation. As shown in Fig. 12 and 13, the shape of the RA increased in length after the tensile test. This implies that most of the RA was deformed first and subsequently transformed into martensite. From the diffraction pattern of the martensite shown in Fig. 12 and 13, two different types of martensite were formed from the deformed RA. The first was the α'-martensite shown in Fig. 12. The second was epsilon martensite (ε-martensite) shown in Fig. 13. The different arrangements of the stacking faults form ε-martensite or mechanical twins depending on the stacking fault energy (SFE) (Ref 48-50). As a metastable phase, ε-martensite is formed at a higher degree of deformation, which is mainly formed in shear bands. The ε-martensite was found to play a key role in the nucleation of α'-martensite in individual shear bands, which was believed to reduce the activation energy needed for α'-martensite nucleation (Ref 51).

5. Conclusion

This study investigates the microstructure and mechanical properties of medium manganese steel with different aluminum additions after IA at different temperatures for an exceedingly brief time of 1 min. The following conclusions can be reached:

1. The addition of aluminum extends the IA temperature range from 338 °C for 1.0 Al to 506 °C for 2.5 Al, which shifted the IA range toward higher temperatures. This has consequently contributed to the excellent mechanical properties of 2.5Al after a very short IA time annealing.
2. The final microstructures after IA at 730 °C (for 1.0 Al) and 790 °C (for 2.5 Al) contained the highest amount of RA, resulting in better tensile properties than those at other IA temperatures. The mechanical properties of 2.5 Al after annealing at 790 °C for 1 min were TS of 982.5 MPa, TEL of 42.96%, and strength × ductility greater than 42.00 GPa%.
3. The RA of the 2.5 Al before the tensile test has two morphologies, namely, polygonal and lath. After the tensile test, the RA transforms into martensite, and there are two different types of martensite, α'-martensite, and ε-martensite.

References

1. J. Zhao and Z. Jiang, Thermomechanical Processing of Advanced High Strength Steels, *Prog. Mater. Sci. Elsevier Ltd*, 2018, **94**, p 174–242. https://doi.org/10.1016/j.pmatsci.2018.01.006
2. Y.K. Lee and J. Han, Current Opinion in Medium Manganese Steel, *Mater. Sci. Technol.*, 2015, **31**(7), p 843–856. https://doi.org/10.1179/1743284714Y.0000000722
3. Z. Zhang, F. Yang, H. Zhang, T. Zhang, H. Wang, Y. Xu, and Q. Ma, Influence of CeO2 Addition on Forming Quality and Microstructure of TiCx-Reinforced CrTi4-Based Laser Cladding Composite Coating, *Mater. Charact.*, 2021, **171**, p 110732. https://doi.org/10.1016/j.matchar.2020.110732
4. L. Liang, M. Xu, Y. Chen, T. Zhang, W. Tong, H. Liu, H. Wang, and H. Li, Effect of Welding Thermal Treatment on the Microstructure and Mechanical Properties of Nickel-Based Superalloy Fabricated by Selective Laser Melting, *Mater. Sci. Eng. A*, 2021, **819**, p 141507. https://doi.org/10.1016/j.msea.2021.141507
5. C.D. Horvath, Chapter 2 - Advanced Steels for Lightweight Automotive Structures, *Woodhead Publishing in Materials*, P.K.B.T.-M. Mallick Design and Manufacturing for Lightweight Vehicles (Second Edition), Ed., Woodhead Publishing, 2021, p 39–95, https://doi.org/10.1016/B978-0-12-818712-8.00002-1
6. H. Ashrafi, M. Shamanian, R. Emadi, S.E. Aghili, and E. Ghassemali, Damage Micromechanisms in Friction Stir-Welded DP600 Steel during Uniaxial Tensile Deformation, *J. Mater. Eng. Perform.*, 2022, **31**(12), p 10044–10053. https://doi.org/10.1007/s11665-022-06978-z
7. F. Eşiyok, R. Ertan, G. Sevilgen, E. Bulut, F. Öztürk, İ Alyay, and T.T. Abi, A Comparative Study on Conventional and Hybrid Quenching Hot Forming Methods of 22MnB5 Steel for Mechanical Properties and Microstructure, *J. Mater. Eng. Perform.*, 2023, **32**(3), p 1347–1356. https://doi.org/10.1007/s11665-022-07167-8
8. Y. Li, R. Wang, B. Wang, W. Ding, Influence of Silicon Addition on Intercritical Annealing Process and Tensile Properties of Medium Mn Steel. *J. Mater. Sci.*, Springer US, 2021, **56**(2), p 1783–1793, https://doi.org/10.1007/s10853-020-05330-x
9. Z. Wang, J. Xu, and J. Li, Mechanical Properties and Fracture Behaviors of Medium-Mn Steels with and without Delta-Ferrite for Different Intercritical Annealing Times, *Mater. Charact.*, 2021, **172**, p 110730. https://doi.org/10.1016/j.matchar.2020.110730
10. Y. Li, F. Huyan, and W. Ding, Microstructure and Tensile Properties of a 0.20C–4.86Mn Steel after Short Intercritical- Annealing Times, *Mater. Sci. Technol.*, 2019, **35**(2), p 220–230. https://doi.org/10.1080/02670836.2018.1550864
11. D.M. Field, J. Qing, and D.C.V.A.N. Aken, Chemistry and Properties of Medium-Mn Two-Stage TRIP Steels. *Metall. Mater. Trans. A*, Springer US, 2018, **49**(10), p 4615–4632, https://doi.org/10.1007/s11661-018-4798-6
12. A. Perlade, A. Antoni, R. Besson, D. Caillard, J. Emo, A. Gourgues, P. Maugis, L. Thuinet, Q. Tonizzo, J. Schmitt, A. Perlade, A. Antoni, R. Besson, D. Caillard, J. Emo, A. Gourgues, P. Maugis, and A. Mestrallet, Development of 3rd Generation Medium Mn Duplex Steels for Automotive Applications, *Mater. Sci. Technol.*, 2019, **35**(2), p 204–219
13. W. Ding, J. Du, and Y. Li, Transformations During Intercritical Annealing and Their Implications for Microstructure and Mechanical Properties of Medium Mn Transformation-Induced Plasticity Steel in Continuous Annealing Line, *J. Mater. Eng. Perform.*, Springer US, 2020, **29**(1), p 23–31
14. H. Lee, M.C. Jo, S.S. Sohn, A. Zargaran, J.H. Ryu, N.J. Kim, and S. Lee, Novel Medium-Mn (Austenite + Martensite) Duplex Hot-Rolled Steel Achieving 1.6 GPa Strength with 20 % Ductility by Mn-Segregation-Induced TRIP Mechanism, *Acta Mater.*, Elsevier Ltd, 2018, **147**, p 247–260, https://doi.org/10.1016/j.actamat.2018.01.033
15. J. Qiu, M. Zhang, X. Liu, X. Zhang, and Z. Tan, Materials Science & Engineering A Characterization of Retained Austenite in a Low Carbon High Strength Mn – Si – Cr Steel, *Mater. Sci. Eng. A*, Elsevier B.V., 2020, **797**(August), p 139985, https://doi.org/10.1016/j.msea.2020.139985
16. J. Liang, Z. Zhao, D. Tang, N. Ye, S. Yang, and W. Liu, Improved Microstructural Homogeneity and Mechanical Property of Medium Manganese Steel with Mn Segregation Banding by Alternating Lath Matrix, *Mater. Sci. Eng. A*, Elsevier B.V., 2018, **711**(July 2017), p 175–181, https://doi.org/10.1016/j.msea.2017.11.046

17. Y. Li, W. Ding, and B. Wang, Intercritical Annealing Pre-Treatment Used in a Hot- Dip Galvanised TRIP Steel, *Mater. Sci. Technol.*, 2019, **35**(11), p 1372–1380. https://doi.org/10.1080/02670836.2019.1625171

18. Z.C. Li, H. Ding, and Z.H. Cai, Mechanical Properties and Austenite Stability in Hot-Rolled 0.2C-1.6/3.2Al-6Mn-Fe TRIP Steel, *Mater. Sci. Eng. A*, 2015, **639**, p 559–566

19. H. Aydin, E. Essadiqi, I.H. Jung, and S. Yue, Development of 3rd Generation AHSS with Medium Mn Content Alloying Compositions, *Mater. Sci. Eng. A*, Elsevier, 2013, **564**, p 501–508, https://doi.org/10.1016/j.msea.2012.11.113

20. H. Xu, W. Cao, H. Dong, and J. Li, Effects of Aluminium on the Microstructure and Mechanical Properties in 0.2 C–5Mn Steels under Different Heat Treatment Conditions, *ISIJ Int.*, The Iron and Steel Institute of Japan, 2015, **55**(3), p 662–669

21. W. Ding, R. Wang, Y. Li, and B. Wang, High Elongation of Medium-Manganese Steel Containing 1.0 Wt.% Al after a Short Intercritical Annealing Time, *J. Mater. Res. Technol.*, 2020, **9**(4), p 7262–7272

22. A.L. Vidilli, L.B. Otani, W. Wolf, C.S. Kiminami, W.J. Botta, F.G. Coury, and C. Bolfarini, Design of a FeMnAlC Steel with TWIP Effect and Evaluation of Its Tensile and Fatigue Properties, *J. Alloys Compd.*, Elsevier B.V, 2020, **831**, p 154806, https://doi.org/10.1016/j.jallcom.2020.154806

23. T. Bhattacharyya, S. Brat, S. Das, A. Haldar, and D. Bhattacharjee, Development and Characterisation of C – Mn – Al – Si – Nb TRIP Aided Steel, *Mater. Sci. Eng. A* Elsevier B.V., 2011, **528**(6), p 2394–2400, https://doi.org/10.1016/j.msea.2010.11.054

24. Z. Deng, M. Zhu, Y. Zhou, and D. Sichen, Attachment of Alumina on the Wall of Submerged Entry Nozzle during Continuous Casting of Al-Killed Steel, *Metall. Mater. Trans. B* Springer US, 2016, **47**(3), p 2015–2025

25. S. Jing, H. Ding, Y. Ren, and Z. Cai, A New Insight into Annealing Parameters in Tailoring the Mechanical Properties of a Medium Mn Steel, *Scr. Mater.* Elsevier Ltd, 2021, **202**, p 114019. https://doi.org/10.1016/j.scriptamat.2021.114019

26. B.D.Cullity and S.R.Stock, "Elements of X-Ray Diffraction(3rd-Edition)," *Prentice Hall*, 2001

27. S. Kang, J.G. Speer, D. Krizan, D.K. Matlock, and E. De Moor, Prediction of Tensile Properties of Intercritically Annealed Al-Containing 0.19C-4.5Mn (Wt%) TRIP Steels, *Mater. Des.*, Elsevier Ltd, 2016, **97**, p 138–146, https://doi.org/10.1016/j.matdes.2016.02.058

28. Kang S, E. De Moor, and J.G. Speer, Retained Austenite Stabilization through Solute Partitioning during Intercritical Annealing in C-, Mn-, Al-, Si-, and Cr-Alloyed Steels, *Metall. Mater. Trans. A*, 2015, **46**(MARCH), p 1005–1011

29. B. Sun, F. Fazeli, C. Scott, N. Brodusch, R. Gauvin, and S. Yue, The Influence of Silicon Additions on the Deformation Behavior of Austenite-Ferrite Duplex Medium Manganese Steels, *Acta Mater.*, Elsevier Ltd, 2018, **148**, p 249–262, https://doi.org/10.1016/j.actamat.2018.02.005

30. D.P. Koistinen and R.E. Marburger, A General Equation Prescribing the Extent of the Austenite-Martensite Transformation in Pure Iron-Carbon Alloys and Plain Carbon Steels, *Acta Metall.*, 1959, **7**(1), p 59–60. https://doi.org/10.1016/0001-6160(59)90170-1

31. S. Lee, S. Shin, M. Kwon, K. Lee, and B.C. De Cooman, Tensile Properties of Medium Mn Steel with a Bimodal UFG α + γ and Coarse δ-Ferrite Microstructure, *Metall. Mater. Trans. A*, 2017, **48**(4), p 1678–1700. https://doi.org/10.1007/s11661-017-3979-z

32. O.A. Zambrano, Review A General Perspective of Fe – Mn – Al – C Steels, *J. Mater. Sci.*, Springer US, 2018, **53**(20), p 14003–14062, https://doi.org/10.1007/s10853-018-2551-6

33. V. Shterner, I.B. Timokhina, and H. Beladi, On the Work-Hardening Behaviour of a High Manganese TWIP Steel at Different Deformation Temperatures, *Mater. Sci. Eng. A*, Elsevier, 2016, **669**, p 437–446

34. W. Püschl, Models for Dislocation Cross-Slip in Close-Packed Crystal Structures: A Critical Review, *Prog. Mater. Sci.*, Elsevier, 2002, **47**(4), p 415–461

35. S. Liu, Z. Xiong, H. Guo, C. Shang, and R.D.K. Misra, The Significance of Multi-Step Partitioning: Processing-Structure-Property Relationship in Governing High Strength-High Ductility Combination in Medium-Manganese Steels, *Acta Mater.*, Elsevier Ltd, 2017, **124**, p 159–172, https://doi.org/10.1016/j.actamat.2016.10.067

36. A. Dumay, J.-P. Chateau, S. Allain, S. Migot, and O. Bouaziz, Influence of Addition Elements on the Stacking-Fault Energy and Mechanical Properties of an Austenitic Fe–Mn–C Steel, *Mater. Sci. Eng. A*, 2008, **483–484**, p 184–187. https://doi.org/10.1016/j.msea.2006.12.170

37. H. Luo and H. Dong, New Ultrahigh-Strength Mn-Alloyed TRIP Steels with Improved Formability Manufactured by Intercritical Annealing, *Mater. Sci. Eng. A*, Elsevier, 2015, **626**, p 207–212, https://doi.org/10.1016/j.msea.2014.12.049

38. J. Shi, X. Sun, M. Wang, W. Hui, H. Dong, and W. Cao, Enhanced Work-Hardening Behavior and Mechanical Properties in Ultrafine-Grained Steels with Large-Fractioned Metastable Austenite, *Scr. Mater.*, Acta Materialia Inc., 2010, **63**(8), p 815–818, https://doi.org/10.1016/j.scriptamat.2010.06.023

39. D.M. Pallisco and J.R. McDermid, Mechanical Property Development of a 0.15C–6Mn–2Al–1Si Third-Generation Advanced High Strength Steel Using Continuous Galvanizing Heat Treatments, *Mater. Sci. Eng. A*, 2020, **778**, p 139111, https://doi.org/10.1016/j.msea.2020.139111

40. H.F. Xu, J. Zhao, W.Q. Cao, J. Shi, C.Y. Wang, C. Wang, J. Li, and H. Dong, Heat Treatment Effects on the Microstructure and Mechanical Properties of a Medium Manganese Steel (0.2C–5Mn), *Mater. Sci. Eng. A*, 2012, **532**(5), p 435–442

41. J. Hu, W. Cao, C. Huang, C. Wang, H. Dong, and J. Li, Characterization of Microstructures and Mechanical Properties of Cold-Rolled Medium-Mn Steels with Different Annealing Processes, *ISIJ Int.*, 2015, **55**(10), p 2229–2236

42. R. Sun, W. Xu, C. Wang, J. Shi, H. Dong, and W.C. Ã, Work Hardening Behavior of Ultrafine Grained Duplex Medium-Mn Steels Processed by ART-Annealing, *Steel Res. Int.*, 2012, **83**(4), p 316–321

43. J. Chiang, B. Lawrence, J.D. Boyd, and A.K. Pilkey, Effect of Microstructure on Retained Austenite Stability and Work Hardening of TRIP Steels, *Mater. Sci. Eng. A*, Elsevier, 2011, **528**(13–14), p 4516–4521, https://doi.org/10.1016/J.MSEA.2011.02.032

44. J. Qiu, M. Zhang, X. Liu, X. Zhang, and Z. Tan, The Study of the Planar Defects of the Nano-Sized Retained Austenite in Mn-Si-Cr Steel, *Mater. Lett.*, Elsevier B.V., 2020, **266**, p 127510, https://doi.org/10.1016/j.matlet.2020.127510

45. S.-J. Lee and K.-S. Park, Prediction of Martensite Start Temperature in Alloy Steels with Different Grain Sizes, *Metall. Mater. Trans. A*, Springer, 2013, **44**(8), p 3423–3427

46. K. Sugimoto, M. Misu, M. Kobayashi, and H. Shirasawa, Effects of Second Phase Morphology on Retained Austenite Morphology and Tensile Properties in a Trip-Aided Dual-Phase Steel Sheet, *ISIJ Int.*, 1993, **33**(7), p 775–782. https://doi.org/10.2355/isijinternational.33.775

47. P. Jacques, Q. Furnémont, T. Pardoen, and F. Delannay, On the Role of Martensitic Transformation on Damage and Cracking Resistance in TRIP-Assisted Multiphase Steels, *Acta Mater.*, 2001, **49**(1), p 139–152

48. Y. Tian, O.I. Gorbatov, A. Borgenstam, A. V. Ruban, and P. Hedström, Deformation Microstructure and Deformation-Induced Martensite in Austenite Fe-Cr-Ni Alloys Depending on Stacking Fault Energy. *Metall. Mater. Trans. A Phys. Metall. Mater. Sci.*, 2017, **48**(1), p 1–7

49. J. Talonen and H. Hänninen, Formation of Shear Bands and Strain-Induced Martensite during Plastic Deformation of Metastable Austenitic Stainless Steels. *Acta Mater.*, Elsevier, 2007, **55**(18), p 6108–6118

50. R.S. Mishra, S.S. Nene, M. Frank, S. Sinha, K. Liu, and S. Shukla, Metastability Driven Hierarchical Microstructural Engineering: Overview of Mechanical Properties of Metastable Complex Concentrated Alloys, *J. Alloys Compd.*, Elsevier BV., 2020, p 155625, https://doi.org/10.1016/j.jallcom.2020.155625

51. G. Sun, M. Zhao, L. Du, and H. Wu, Significant Effects of Grain Size on Mechanical Response Characteristics and Deformation Mechanisms of Metastable Austenitic Stainless Steel, *Mater. Charact.*, 2022, **184**, p 111674. https://doi.org/10.1016/j.matchar.2021.111674